Nanoscale
Advances

PAPER

View Article Online
View Journal | View Issue

Check for updates

Cite this: *Nanoscale Adv.*, 2025, 7, 5637

Defect identification in monolayer $MoTe_2$ through tunneling tip-induced charging and theoretical analysis

Pablo Casado,[ab] Michele Pisarra,[ac] Fabian Calleja,[a] Cristina Díaz,[d] Fernando Martín,[ae] Amadeo L. Vázquez de Parga[abfg] and Manuela Garnica[*ag]

Received 21st May 2025
Accepted 3rd August 2025

DOI: 10.1039/d5na00501a

rsc.li/nanoscale-advances

Defects in transition metal dichalcogenides (TMDs) are pivotal in modulating their electronic, optical, and catalytic properties. Investigating these defects is essential for advancing both fundamental knowledge and practical applications. In this study, we examine the individual defects in a monolayer of $MoTe_2$ supported on graphene grown on an Ir(111) substrate by means of scanning tunneling microscopy (STM). Charging rings appear at distinct bias voltages, revealing ionization levels of doping centers located either below or above the Fermi level. Although direct STM visualization of point defects was not achieved, the combination of scanning tunneling spectroscopy (STS) and density functional theory (DFT) calculations enabled the identification of the structural origins of the charge states. Our results demonstrate a powerful tool for uncovering the electronic and structural characteristics of atomic-scale defects in $MoTe_2$, contributing to the understanding of defect-driven electronic properties in transition metal dichalcogenides.

1 Introduction

Single atomic impurities within 2D semiconductor materials have emerged as critical factors in determining their electronic properties. The ability to control atomic defects and understand their role in the optoelectronic structure, is then essential for the practical application of these materials in next-generation electronic devices.[1] In transition metal dichalcogenides (TMDs), chalcogen vacancies are common defects, often leading to the formation of anti-site defects that can accommodate a variety of dopants. These defects are known to introduce new electronic states within the bandgap,[2] significantly impacting their carrier mobility and overall performance.[3] In addition, oxygen substitution has been demonstrated to be the most abundant point defect in chemical vapor deposition (CVD)-grown samples, effectively passivating the gap states.[4,5] Recent progress has been made in understanding the impact of point defects in TMDs, particularly in the 1H-MoX_2 family (where X = Te, Se, S). For example, a chalcogen vacancy in MoS_2 and $MoSe_2$ typically results in a change in the local electronic density of states, which can further affect the material's conductivity and reactivity[6–10]

Scanning tunneling microscopy (STM) has proven to be an invaluable tool for identifying these atomic-scale defects,[4,11] and it has also been demonstrated that the charge state of individual donors can be dynamically manipulated with high precision using an STM tip,[12] enabling detailed studies of defect behavior at the atomic level. Notably, defects have been observed to adopt negative charge states through tip-induced gating effects in WSe_2 grown on BLG/SiC(0001),[13] $PdSe_2$,[14,15] or MoS_2 [16] crystals.

While considerable research has focused on transition metal disulfides and selenides, transition metal tellurides have received comparatively less attention. Here, we use an STM to study the charging of single defects in a monolayer of $MoTe_2$ supported on a graphene monolayer grown on the Ir(111) surface. Differential conductance spectroscopy (dI/dV) reveals charging rings at various bias voltages. The ionization levels of the doping centers, located either below or above the Fermi level, respond differently to applied bias voltages. Although direct visualization of the point defects by STM has not been achieved, the combination of scanning tunneling spectroscopy (STS) and density functional theory (DFT) calculations allows us to deduce the structural origins of the observed charge states.

---

[a] *Instituto Madrileño de Estudios Avanzados en Nanociencia (IMDEA-Nanociencia), 28049 Madrid, Spain. E-mail: manuela.garnica@imdea.org*

[b] *Departamento de Física de la Materia Condensada, Universidad Autónoma de Madrid, 28049 Madrid, Spain*

[c] *Dipartimento di Fisica, Università della Calabria and INFN, Gruppo Collegato di Cosenza, 87036 Rende, CS, Italy*

[d] *Departamento de Química Física, Universidad Complutense de Madrid, 28040 Madrid, Spain*

[e] *Departamento de Química, Universidad Autónoma de Madrid, 28049 Madrid, Spain*

[f] *Condensed Matter Physics Center (IFIMAC), Universidad Autónoma de Madrid, 28049 Madrid, Spain*

[g] *Instituto "Nicolás Cabrera", Universidad Autónoma de Madrid, 28049 Madrid, Spain*

2 Methods

The sample preparation begins with the cleaning of the crystal. First, the Ir(111) surface was prepared by three cycles of Ar^+ sputtering followed by flash annealing at 1650 K, 1600 K and 1550 K. With this treatment a flat and clean Ir(111) surface is obtained. Then, in order to grow the graphene (gr) layer, the sample is exposed to a partial pressure of 5×10^{-8} mbar of ethylene (C_2H_4) while it is held at 1450 K during seven minutes, resulting in a dosage of 12.6 L. Finally, the sample is held an additional minute at 1450 K without the ethylene atmosphere in order to homogenize the sample. This procedure results in a complete monolayer of graphene on the Ir(111) surface with the gr and Ir lattices aligned, leading to an incommensurate (9 × 9) moiré pattern.[17]

After the gr/Ir(111) preparation, $MoTe_2$ was grown by molecular beam epitaxy (MBE). Elemental Mo (99.9+% purity) is evaporated from an e-beam evaporator while elemental Te (99.999% purity) is evaporated using a resistive heating evaporator. $MoTe_2$ islands were grown by exposing the hot gr/Ir(111) sample during 20 min to a Te : Mo ratio of the order of 12 : 1. Depending on the sample temperature during the growth, we have shown that two different phases can be obtained.[18] Once the growth was complete, the sample underwent a long annealing step at the same temperature for about one hour.

The differential conductance (dI/dV) was determined using lock-in detection of the AC tunneling current, achieved by modulating the sample bias (763 Hz) measuring in constant height mode with the feedback loop open. All measurements were carried out at 1.2 K. STM images were analyzed using WxSM[19] and Gwyddion[20] software.

DFT calculations have been carried out using the PAW method[21] as implemented in the VASP package.[22–24] We used the PBE[25] exchange–correlation functional, 400 eV for the plane wave cut-off, and a 10^{-5} eV energy convergence criterion in the electronic self consistent cycles. We also included the Tkatchenko–Scheffler[26] van der Waals correction, which proved to be very effective in reproducing the effects of weak dispersion forces in hexagonal transition metal dichalcogenides materials.[27]

The minimal (1 × 1) unit cell of 1H-$MoTe_2$ contains one Mo atom, which is located at the center of a triangular right prism, whose vertices are occupied by Te atoms; in this way, a total of 2 Te atoms are contained in the (1 × 1) unit cell. For the defect calculations, a convergence study has been carried out over the lateral size of the supercell. We carried out calculations for (3 × 3), (5 × 5), (7 × 7), (9 × 9), and (11 × 11) supercells, constructed starting from the nominal optimized (1 × 1) unit. Once the given defect was created, for the supercell size up to (7 × 7), we have optimized the coordinates of all the atoms within a (5 × 5) cell surrounding the defect. The (9 × 9), and (11 × 11) results are obtained from single-point DFT calculation using the coordinates of the (7 × 7) supercell and adding the additional atoms in their nominal optimized positions. Finally, we also took into account the effect of the supporting substrate. The gr–Ir surface was modeled constructing a (10 × 10) graphene layer over a (9 × 9) three-layer-thick Ir(111) slab, optimizing the coordinates of all C atoms, and of the topmost Ir layer. The nominal lateral size of the unit cell for this system, dictated by the (9 × 9) Ir(111) substrate, is $L_{\text{gr–Ir}} = 24.629$ Å, which entails a negligible stress on the graphene layer. We observe that the (7 × 7) $MoTe_2$ supercell has a nominal lateral size of $L_{(7\times7)\text{MoTe}_2} = 24.710$ Å, which differs by less than 0.3% from the one of gr–Ir. Hence we placed a (7 × 7) $MoTe_2$ monolayer (with and without defect) on one side of the gr–Ir system, using the $L_{(7\times7)\text{MoTe}_2}$ and re-optimized the Mo, Te and C atoms coordinates. All the geometry optimizations have been carried out until the residual force on the active atoms was lower than 0.01 eV Å^{-1}. In all calculations, we included at least a 20 Å vacuum region in the out-of-plane direction. Depending on the lateral size of the supercell, different k-point meshes have been adopted to sample the Brillouin Zone, characterized by $\Delta k \leq 0.1$ Å^{-1}.

A key factor in calculating the defect formation energy (*cf.* eqn (3)) is the chemical potential of the added/removed atoms. An upper limit (in absolute value) for this quantity can be determined as the energy per atom in the most stable bulk allotrope of the material. This can be estimated by a DFT calculation using the same settings as given above, yielding $\mu_{\text{Mo}}^{\text{DFT}} = -12.336$ eV and $\mu_{\text{Te}}^{\text{DFT}} = -3.371$ eV. However, for our particular case we need the values of the energy per atom of Mo (E_{Mo}) and Te (E_{Te}) in a $MoTe_2$ compound in the hexagonal phase. These quantities can be derived, for instance, from the bulk 2H-$MoTe_2$ system. In a bulk 2H-$MoTe_2$ system, which contains two Mo atoms and four Te atoms per unit cell, the total energy per unit cell can be expressed as $E_{\text{2H-MoTe}_2} = 2E_{\text{Mo}} + 4E_{\text{Te}} + \Delta H$, where ΔH represents the formation hentalpy of the compound. By performing a DFT calculation of the bulk 2H-$MoTe_2$ we obtain the total energy for bulk $MoTe_2$ at the DFT level, $E_{\text{2H-MoTe}_2}^{\text{DFT}}$, and the chemical potentials are then refined as follows:

$$\mu_{\text{Te}} = \frac{E_{\text{2H-MoTe}_2}^{\text{DFT}} - \Delta H_{\text{MoTe}_2}}{4 + 2\dfrac{\mu_{\text{Mo}}^{\text{DFT}}}{\mu_{\text{Te}}^{\text{DFT}}}} = -3.282 \text{ eV}, \tag{1}$$

$$\mu_{\text{Mo}} = \frac{E_{\text{2H-MoTe}_2}^{\text{DFT}} - \Delta H_{\text{MoTe}_2}}{4 + 2\dfrac{\mu_{\text{Mo}}^{\text{DFT}}}{\mu_{\text{Te}}^{\text{DFT}}}} \frac{\mu_{\text{Mo}}^{\text{DFT}}}{\mu_{\text{Te}}^{\text{DFT}}} = -12.012 \text{ eV}, \tag{2}$$

where the experimental value[28] $\Delta H_{\text{MoTe}_2} = 0.936$ eV is used as the formation enthalpy of bulk $MoTe_2$ in the 2H phase.

3 Results

3.1 STM-STS characterization

Recently, we have demonstrated the feasibility of phase engineering of $MoTe_2$, enabling the growth of islands in its semiconducting 1H phase.[18] Fig. 1 presents an STM image of a 1H-$MoTe_2$ island, revealing linear defects oriented at 60° angles. These one-dimensional defects are known as mirror twin boundaries (MTBs), because they separate two domains that are mirrored versions of each other. MTBs are a characteristic feature observed in nearly all 1H-TMDs and are especially

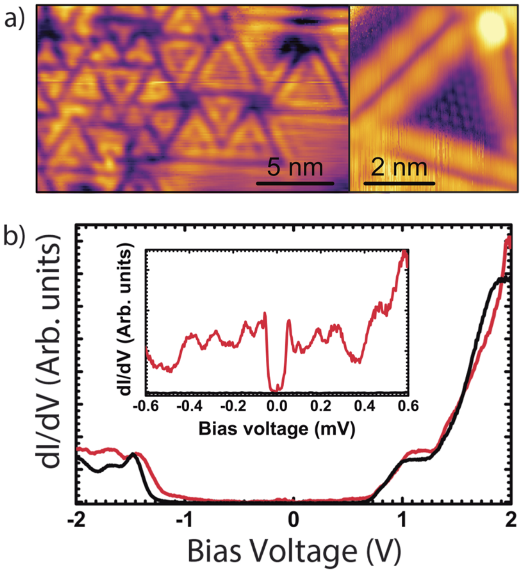

Fig. 1 (a) Left panel: STM image of a 1H-MoTe$_2$ region with a high density of MTBs ($V_b = 1$ V and $I_t = 0.1$ nA). Right panel: Zoom in on one of the MTB-loops. (b) Individual dI/dV curves measured in the MTB-rich region (red curve) and in the pristine 1H-MoTe$_2$ region (black curve). In the MTB region, the bandgap is reduced, and distinct in-gap features are observed. Measurements performed at $T = 1.2$ K.

prevalent in those containing Mo.[29] In the case of MoTe$_2$, the abundance of MTBs is particularly notable due to the facile incorporation of excess Mo atoms into the lattice.[29–31]

As illustrated in Fig. 1, MTBs of varying lengths are observed, with shorter boundaries being more prevalent. The high density of these MTBs hampers the precise atomic identification of the underlying 1H-MoTe$_2$ lattice. However, within some of the domains delineated by these MTBs (Fig. 1(a)), it is possible to obtain atomically resolved STM images, as shown also in Fig. S1 in the SI. In these regions, the measured lattice constant is 3.45 ± 0.09 Å, corresponding to the expected atomic spacing of the 1H-MoTe$_2$ structure.

To investigate the effect of MTBs on the electronic structure of 1H-MoTe$_2$, we have carried out STS measurement on our sample. The red curve in Fig. 1(b) is a dI/dV measurement corresponding to the left region shown in Fig. 1(a), which contains a high density of MTBs. The black curve has been acquired on pristine 1H-MoTe$_2$ (right corner of the STM image in Fig. 1(a)), and is used as reference. In both cases, we have a gap of around 2.0 eV, which allows us to observe that the MoTe$_2$ monolayer is slightly n-doped due, possibly, to charge transfer from defects. The most notable difference between the two curves is the presence of in-gap features within the semiconducting bandgap in the MTB-rich area, including narrow peaks as illustrated in the shorter-range STS shown in the inset of Fig. 1(b). Moreover, a clear modulation of the local density of states (LDOS) along each MTB is visible in Fig. 1(a) and S2 in the SI. This has been reported and investigated before for MoTe$_2$ and other molybdenum dichalcogenides[29] and attributed to the formation of a 1D Peierls-type CDW[31,32] or Tomonaga–Luttinger liquid.[33–35]

Additionally, in several 1H-MoTe$_2$ islands, peculiar features, at specific bias voltages, are observed in the STS. Fig. 2(a) shows an island in which a grid spectroscopy measurement was performed. In Fig. 2(b), the dI/dV spectra acquired at the locations marked by the blue and red circles in Fig. 2(a) are reported. These spectra, in addition to the MTB-related in-gap states, exhibit very intense and narrow peaks at −255 mV and 262 mV. We attribute these peaks to charged states, which are also detected in the surrounding areas as bright rings that emerge at particular bias voltages, as observed in dI/dV images at 308 mV and −290 mV shown in Fig. 2(c and d), respectively. Note that, due to the growth procedure, the vast majority of 1H regions in our sample are MTB-rich[18,29] and, hence, the STS data we use to study the charging rings comes from them. However, based on the similarities with the MoS$_2$ system,[16] we expect a similar behavior in pristine 1H.

Interestingly, the diameter of the rings changes with the bias voltage, increasing as the STM tip moves farther from the center of the ring at a given tip-sample distance. A very direct way to visualize this effect is by taking a line profile across both rings (yellow arrows in Fig. 2(c and d)) and represent every dI/dV curve along the line in a 2D plot as that shown in Fig. 2(e). The y-axis indicates the distance from the beginning of the line profile while the x-axis denotes the bias voltage, thus being the intensity of the dI/dV signal represented by the color scale (brighter means higher intensity). The positions of the peaks exhibit a parabolic trend in this representation, indicating a shift in energy as the tip moves farther away from the center.

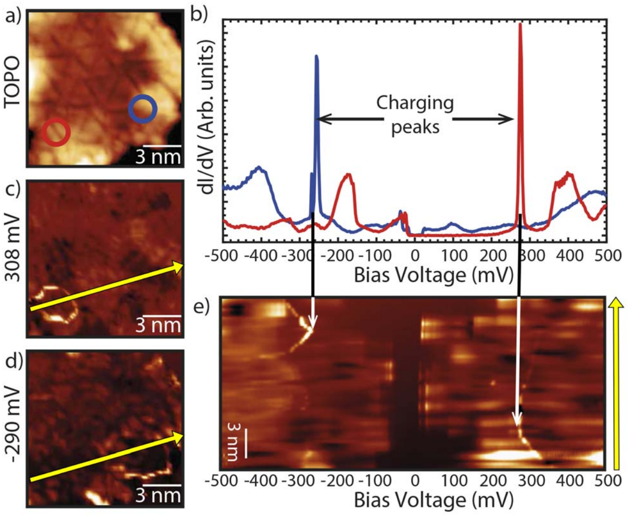

Fig. 2 (a) STM image ($V_b = 0.5$ V and $I_t = 0.5$ nA) where a grid spectroscopy ($V_b = -0.5$ V, $I_t = 0.5$ nA and $V_{mod} = 3$ mV) was measured. From it, dI/dV curves at the locations of the red and blue circles in (a) are extracted, where two narrow peaks can be seen. (c and d) are dI/dV maps at the energies of the peaks from (b), where the charge rings are clearly visible. (e) 2D representation of dI/dV curves taken along the yellow arrows depicted in (b and c), where the color scheme represents the intensity of the lock-in signal. The displacement in energy of the charging peaks (brighter features) as well as the ring diameters can be tracked in this representation. Measurements performed at $T = 1.2$ K.

This kind of feature has already been observed in STM experiments for a wide variety of systems due to the presence of impurities or defects such as metallic adatoms on topological insulators[36,37] or graphene,[38] organic molecules on hexagonal boron nitride,[39,40] vacancies on the surface of several TMD crystals[2,14–16,41] or individual point-defect states buried in the bilayer WSe_2.[13] They are usually attributed to states lying inside the semiconducting bandgap of the material. These defects change their charge state due to the electric field produced by the applied bias voltage between the STM tip and the sample. Specifically, the electric field created by the tip produces a bending of the electronic bands of the material known as tip induced band bending (TIBB).[39] This bending also affects the state of the defect, which changes its charge nature when the respective band crosses the Fermi level[39] as sketched in Fig. 3. This crossing gives rise to sudden changes in the tunneling current and, therefore, to narrow peaks in the STS signal, as seen in Fig. 2(b). As the intensity of the electric field depends on the tip-defect distance, the strength of such bending will also depend on the tip location, being maximum when the tip is right on top of the defect (see Fig. 3(a and b)).

When the tip is located at a certain lateral distance from the defect, the effect on the electronic state associated to the defect (E_D) is weaker: a stronger field (higher bias voltage) is needed to induce the crossing of the Fermi level. Therefore, for a given sufficiently high bias, there exists a certain tip-defect distance at which the latter gets charged, giving rise to the charging rings as the one sketched in Fig. 3(c).

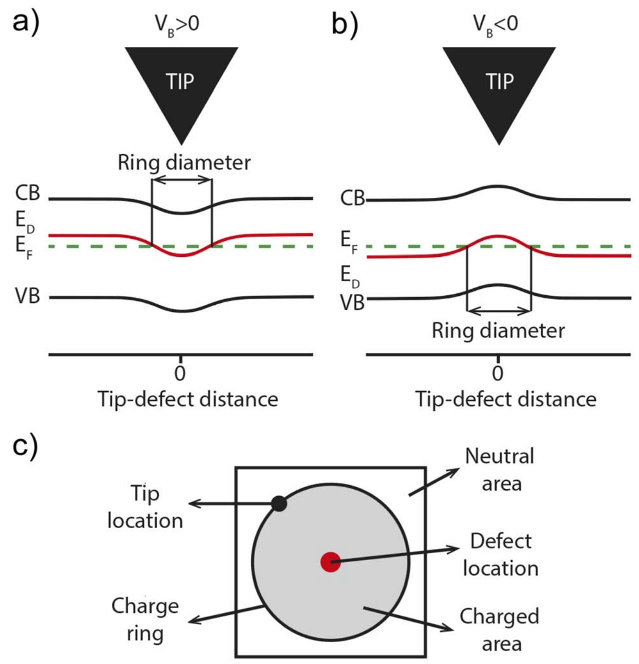

Fig. 3 Tip induced band bending (TIBB) and charge ring schemes. (a) and (b) Schematic representation of the TIBB effect which bends the band structure of the material (CB and VB) as well as those states created by defects (E_D) for positive (a) and negative (b) bias voltages. The charge/discharge of those states occurs when it crosses the Fermi level. (c) Schematic representation of the charge ring created by a charge defect.

The diagrams in Fig. 3 further suggest that TIBB and the appearance of the charging peaks is a threshold phenomenon. This implies the existence of a threshold voltage at which the defect state crosses the Fermi level, thereby altering its charge state. This can be clearly visualized in the series of dI/dV images given in Fig. 4(a–d). In Fig. 4(a), acquired at a bias voltage of 240 mV, the white circle highlights the position of a defect in its natural state. As the applied bias voltage is increased, E_D crosses the Fermi level, giving rise to the charge peak, which appears as a bright spot in Fig. 4(b). If the bias is increased further the charging of the defects still takes place and the specific bright peak associated to E_D crossing the Fermi level happens for a given tip-defect lateral distance, which in Fig. 4(c and d) appears as a bright ring centered at the defect location and characterized by a bias dependent diameter.

Fig. 4(e) presents the evolution of the ring diameter for seven different charge states as encountered in Fig. 2(a) and in other images acquired under similar conditions as Fig. S3. Although several MTBs are present and they are metallic, the net charge associated with them does not appear to be sufficient to induce band bending, and the charge rings are not perturbed by their local electrostatic environment. From the plot, it is clear that the defects are in different initial states, since they appear at opposite polarities (4 at positive and 3 at negative biases). The three defects observed at negative biases appear to be of the same nature, as they appear at the same bias ~ -0.26 V. Two of these defects exhibit nearly identical bias-dependent slopes, indicating comparable interactions with the local electrostatic environment. However, the third defect displays a lower slope. This discrepancy likely arises from differences in the tip shape. A blunter tip distributes the electric field more evenly over a larger area, reducing the strength of TIBB and consequently, leading to a more gradual expansion of the charge rings with bias. In contrast, a sharper tip generates a more localized and intense electric field, leading to stronger TIBB. As a result, the charge rings might show a steeper slope in diameter *vs.* bias. Similarly, on the positive side of the graph, there is a pair of charge states originating from the same type of defect, changing their charge status at ($V_b \sim 0.26$ V) and another pair that appears to be more sensitive to TIBB, as they become charged at a lower voltage ($V_b \sim 0.1$ V), while having a comparable slope to that of the other charge states. Notably, when more than one charge ring appears at unoccupied states, they overlap and interact, forming a common wavefront. Fig. S3 illustrates a 1H-$MoTe_2$ island with multiple defects where a current imaging tunneling spectroscopy (CITS) measurement was conducted. The corresponding dI/dV maps reveal the overlapping of distinct charge rings associated with different defects, suggesting that the defects belong to the same layer. This contrasts with the case of $PdSe_2$,[14,15] where charge rings do not interact because they are produced by defects located in different layers.

3.2 DFT calculations

To clarify the nature of the defects that give rise to the charging peaks, we have performed DFT calculations. The first output of

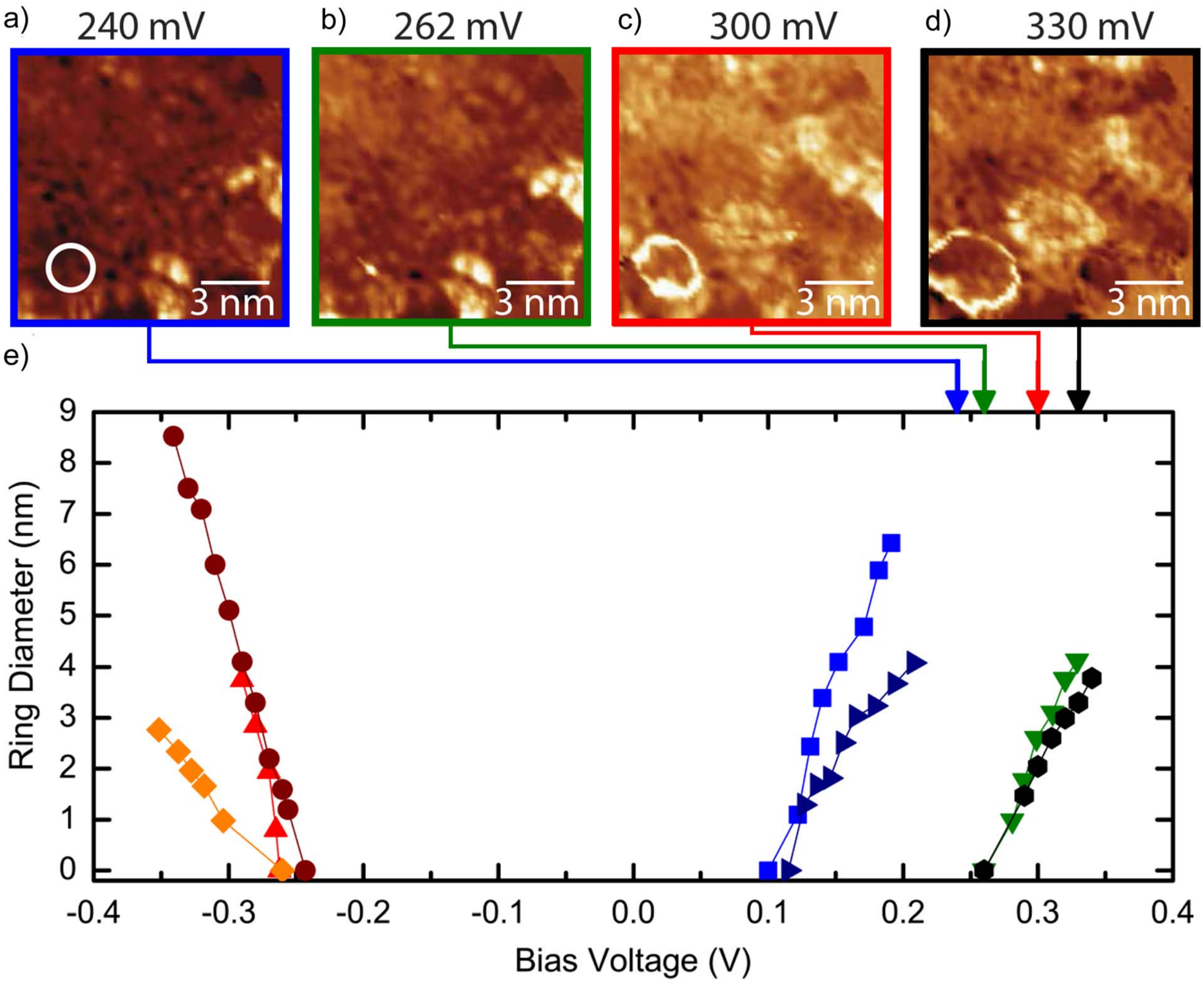

Fig. 4 Charge rings diameters in 1H-MoTe$_2$. (a–d) dI/dV maps showing the evolution of a charge state located at the center of the white circle in (a) from its initial state to the charged one in which the charge peak appears as bright rings (set point $V_b = 0.5$ V and $I_t = 0.5$ nA). (e) Representation of the diameters of the charge rings *vs.* voltage of seven charge states present in the grid spectroscopy of Fig. 2 and in other images acquired under similar conditions as Fig. S3. Measurements performed at $T = 1.2$ K.

the DFT study is the defect formation energy FE$_{\text{Def}}$, which, for neutral system is estimated as:[42]

$$\text{FE}_{\text{Def}} = E_{\text{Def}} - E_{\text{Nom}} - \sum_i n_i \mu_i + E^{\text{int}}_{\text{Def-Def}} \tag{3}$$

In eqn (3) E_{Def} and E_{Nom} are, respectively, the total energies of the system with and without the defect; these two quantities are directly obtained through DFT calculations. n_i is a positive (negative) integer, corresponding to the number of added (removed) atoms of the ith species upon the formation of the defect. These atoms are characterized by the chemical potential μ_i, which can be estimated through DFT, as indicated in the Methods section. Finally, $E^{\text{int}}_{\text{Def-Def}}$ is the interaction energy between defects. $E^{\text{int}}_{\text{Def-Def}}$ is not known in principle and depends on the typical distance between neighboring defects. In our case the $E^{\text{int}}_{\text{Def-Def}}$ contribution to the formation energy can be reduced by increasing the size of the unit cell, inherent to the periodic approach used in this work. Here, we set $E^{\text{int}}_{\text{Def-Def}} = 0$ in eqn (3) and perform a convergence study on the lateral size of the supercell. Converged results are obtained when FE$_{\text{Def}}$ does not change as the size of the supercell is increased. It is important to point out that, given the definition in eqn (3), FE$_{\text{Def}}$ represents the energy absorbed by the system upon the formation of the defect and it is, in general, a positive quantity. Defects with low FE$_{\text{Def}}$ are energetically more probable.

In this work, we analyzed five types of defects: (i) a Mo vacancy; (ii) a Te vacancy; (iii) a Mo–Te substitution, where a Mo atom is replaced by a Te atom; (iv) a Te–Mo substitution, where a Te atom is replaced by a Mo atom; these exhaust all the possibilities of point defects made of only one atom and involving Mo and Te elements; (v) a Mo–Te inversion (where the initial positions of a Mo–Te pair are swapped). Additionally, we have considered the possibility of having (vi) Mo and (vii) Te adatoms either on top of the MoTe$_2$ surface or trapped between MoTe$_2$ and graphene. The presence of trapped charges has led to charge rings due to the electrostatic interaction between doping centers and, for instance, a monolayer of C$_{60}$ molecules supported on a thin Al$_2$O$_3$ film on NiAl(110).[43] Table 1 presents

Table 1 Formation energies FE_{Def} in eV for different supercell sizes and defect types; for the $MoTe_2$ supported by gr/Ir(111) the up (down) arrows marks the result for the case in which the defect was facing the gr–Ir surface (vacuum), when applicable

		(3 × 3)	(5 × 5)	(7 × 7)	(9 × 9)	(11 × 11)	(7 × 7)/gr–Ir
(i)	Mo vacancy	2.970	3.265	3.284	3.292	3.285	3.29
(ii)	Te vacancy	2.560	2.478	2.475	2.485	2.459	2.62 (↑) 2.55 (↓)
(iii)	Te–Mo substitution	3.566	3.482	3.447	3.467	3.464	3.44
(iv)	Mo–Te substitution	4.969	4.967	4.961	4.974	4.968	4.43 (↑) 4.65 (↓)
(v)	Mo/Te inversion	6.022	7.008	6.996	7.004	6.996	5.74 (↑) 5.98 (↓)
(vi)	Mo adatom	6.363	6.396	6.431	6.439	6.430	6.21 (↑) 3.67 (↓)
(vii)	Te adatom	0.881	0.930	0.937	0.936	0.939	0.97 (↑) 3.57 (↓)

the formation energies of these defects and adatoms, calculated using DFT with varying lateral supercell sizes for a freestanding $MoTe_2$ monolayer. The final geometries for the (7 × 7) supercell in a region close to the defect location and the adatoms absorption sites are shown in Fig. S4 and S5 on the SI, respectively. The final column in Table 1 also provides DFT calculated formation energies for defects and adatoms in a $MoTe_2$ monolayer supported by a gr/Ir(111) surface. When applicable, we examine both cases: when the defect is directly in contact with the gr/Ir(111) surface and when it faces the vacuum.

The calculated FE_{Def} shows that, for a (7 × 7) supercell, the $E^{int}_{Def-Def}$ interaction energy is negligible. Indeed, no significant differences are observed in formation energies across the (5 × 5), (7 × 7), (9 × 9), and (11 × 11) supercells. Among the defects, the Te adatoms on top of $MoTe_2$ is the most stable followed by the Te vacancy, with a formation energy of ~0.9 and ~2.5 eV, respectively. The Mo vacancy and Mo–Te substitution have similar formation energies, roughly 1 eV higher than that of the Te vacancy. For comparison, the formation energy of a single vacancy in silicon is ~4 eV.[44] A higher formation energy (~5 eV) was found for the Mo–Te substitution. Finally, the Mo–Te inversion has the highest FE_{Def}, among the defects analyzed in this work. The gr/Ir(111) supporting substrate slightly affects the formation energies, but it does not change the overall energetic scenario in the case of the point defect and when the adatoms are placed on top of the $MoTe_2$ layer. The gr/Ir(111) substrate, on the other hand, has a much stronger impact on the FE_{Def} in the adatom case when the adatom is trapped between the $MoTe_2$ and graphene layer. For the Te adatom, the FE_{Def} increases up to ~3.6 eV. Interestingly, for the Mo adatom, the defect energy is reduced by the substrate to ~3.6 eV.

Fig. 5 reports the density of states (DOS) for the computed $MoTe_2$ (freestanding (7 × 7) cell) in an energy region close to the band gap (wide energy range DOS plots are available in Fig. S6 of the SI). Notably, despite having the lowest formation energy among all defects, the Te adatom does not introduce any in-gap states in $MoTe_2$. In all the other cases, the presence of the defect induces the emergence of in-gap states, that appear as peaks in DOS within the band gap. Interestingly, the DOS for the Te vacancy defect has a single empty peak close to the bottom of the conduction band. On the other hand, all the other defects are characterized by multiple peaks in the gap region of $MoTe_2$, with some of these in-gap-states being filled and other empty. The position and filling of these in-gap states can be, in principle, influenced by the presence of the supporting substrate. The Ir substrate, being metallic, can act as a charge reservoir, which can be efficiently transferred to the $MoTe_2$ layer by graphene, as shown in other graphene supported systems.[45]

However, as shown in Fig. S7 of the SI, the presence of the substrate does not change significantly the qualitative appearance of the $MoTe_2$ derived DOS. Apart from an overall smoothing of the DOS features, we point out three main results.

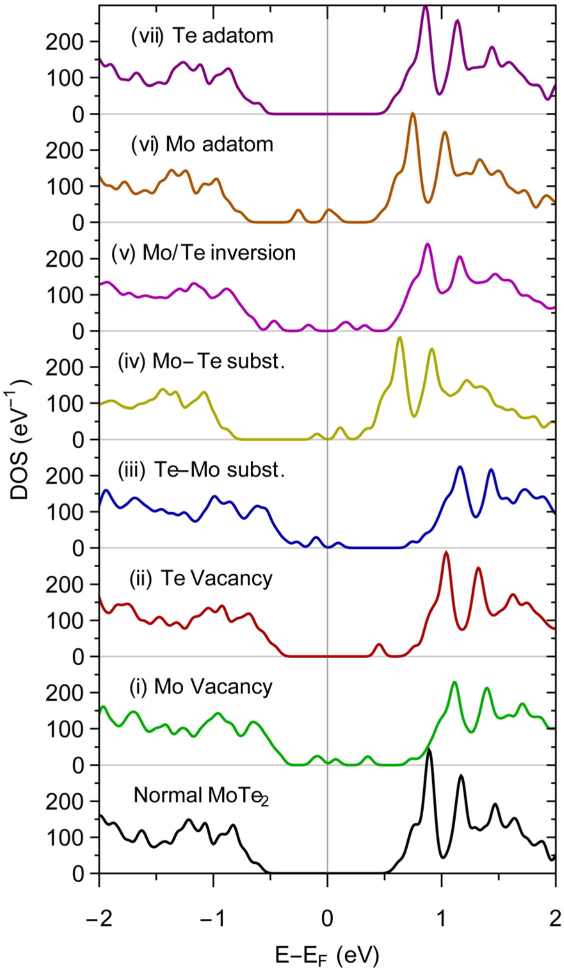

Fig. 5 DFT calculation results. DOS for the calculated defects in a energy region close to the band gap. The Fermi level is set at the midpoint of the gap.

First, regardless of the position of the Te vacancy, this system still has a clear empty state derived from the defect. Second, for the Te–Mo substitution defect, charge transfer from the substrate partially fills one of the in-gap states. Third, the Mo adatom trapped has a DOS characterized by a filled mid gap peak.

3.3 Discussion

$MoTe_2$ exhibits a high density of MTBs due to its ability to incorporate excess Mo and the low formation energy of these defects;[29] however, this does not preclude the presence of point defects, which can still form and coexist with the MTBs. From the experimental results collected in Fig. 2 and 4, we can conclude that there are at least two types of defects in our sample of 1H-$MoTe_2$: one that accepts electrons and another that loses them. Although multiple high-resolution STM images have been taken in areas with charge states, the strong contributions from the metallic MTBs make identifying the structural nature of these charge states challenging. By only looking at the formation energy, the Te adatom is the energetically favored defect, but, since it does not have in-gap states, it cannot be linked to the observed charging rings.

Based on the theoretical defect energy calculations, one can imagine that Te vacancies are also very likely. Additionally, experiments have also shown that chalcogen vacancies can be created in various TMDs by annealing, which is a necessary process during the growth of $MoTe_2$. We further observe that the Te vacancy defect is characterized by an empty in-gap state, which can be filled by TIBB at positive biases. Assuming that the charge defects observed at positive biases are of the same nature, the variation in the TIBB suggests that the defects are located at different vertical distances from the STM tip. The defects that change the charge state at lower bias are likely located in upper layers, while those that change at higher bias are buried deeper, requiring a higher voltage to compensate for the greater tip-to-defect distance in order to feel the same electric field. This requirement is also met by the Te vacancy defect. For these reasons, we can assign the observed defect with charging peaks at positive biases to Te vacancies.

The charging states at negative biases could tentatively be assigned to the Te–Mo substitution.

Although both the Mo vacancy defect and the Te–Mo substitution defect have relatively low formation energies, the DFT calculated DOS for the Mo vacancy defect shows in-gap states that are both filled and empty. It is important to stress that such a defect would, in principle, exhibit charging states at both positive and negative biases—a behavior that has not been observed experimentally. However, the Te–Mo substitution defect displays a state at negative bias and another slightly above the Fermi level. As observed in the STS data of Fig. 1, contrary to freestanding 1H-$MoTe_2$, the system exhibits n-type doping, likely due to charge transfer resulting from the presence of multiple metallic MTBs. This charge transfer could, in principle, cause in-gap states computed to be slightly above the Fermi level (see Fig. 5), actually be just below it. Consequently, Te–Mo substitution defects would display only a filled in-gap state, leading to TIBB charging peaks at negative biases. We observe that Mo adatoms trapped between $MoTe_2$ and graphene are also characterized by a filled in-gap state and have a comparable FE_{Def} to the Mo–Te substitution defect. In principle, this type of defect is a good candidate for the TIBB charging peaks at negative bias. However, this system is unlikely to occur experimentally when growing the samples by MBE. This is because during the deposition of Mo, the sample is heated, which promotes the diffusion of atoms in the weakly interacting graphene layer,[46] favoring their incorporation into the $MoTe_2$ layer and reducing the chances of such trapping occurring in the interface. Therefore, the charge states detected at negative biases are most likely linked to Te–Mo substitution.

We finally point out that we have limited our analysis to point defects made of Mo and Te atoms only. We cannot rule out that other point defects are formed in our 1H-$MoTe_2$ system due to the presence of other elements and contaminants. However we find this possibility unlikely because MBE samples have not been reported in the literature to contain other contaminants, as is often the case with CVD or transferred TMD layers.[4]

4 Conclusions

The growth process of 1H-$MoTe_2$ allows for the incorporation of an excess of Mo atoms, leading to the formation of MTB-loops. These loops exhibit charge modulation that complicates atomic identification through STM. However, STS reveals several point defects through the appearance of sharp and intense conductance peaks at both positive and negative bias polarities. The evolution of these peaks with the bias voltage can be correlated to a tip gating effect. While direct visualization of these defects *via* STM has proven challenging, the combination of STS measurements and DFT calculations provides critical insight into their structural origins. Specifically, the identified defects are associated with Te–Mo substitution and Te vacancies in the upper or lower chalcogen layers of 1H-$MoTe_2$. The nature of these defects can be inferred from their manifestation in the form of rings in the dI/dV at negative or positive bias. Our research presents a method for uncovering the electronic and structural characteristics of atomic-scale defects in $MoTe_2$. This work contributes to a deeper understanding of how these defects influence the electronic properties of TMDs, paving the way for future advancements in the manipulation and control of defect-driven functionalities in these materials.

Author contributions

M. G. conceived the idea. A. L. V. P., F. C. and M. G. planned the experiments. P. C. A., F. C. and M. G. performed the STM experiments and analyzed the data. M. P., C. D. and F. M. performed the DFT calculations. P. C., M. P. and M. G. wrote the manuscript. All authors reviewed and contributed to the manuscript.

Conflicts of interest

There are no conflicts to declare.

Data availability

The data supporting this article have been included as part of the SI and in this document.

Additional data include STM/STS measurements on $MoTe_2$ islands, analysis of mirror twin boundaries (MTBs), and additional density functional theory (DFT) results. These provide further structural, electronic, and theoretical support for the conclusions of the main text. See DOI: **https://doi.org/10.1039/d5na00501a**.

Acknowledgements

The authors acknowledge support by the Spanish Ministry of Science and Innovation and by the "European Union" (Grant no. PID2021-123776NB-C21, PGC2018-096955-B-C44 and PID2021-128011NB-I00, PID2022-138288NB-C31, PID2022-138288NB-C33). IMDEA Nanociencia and IFIMAC acknowledge financial support from the Spanish Ministry of Science and Innovation 'Severo Ochoa' (Grant CEX2020-001039-S) and 'María de Maeztu' (Grant CEX2018-000805-M) Programme for Centres of Excellence in R&D, respectively. Financial support through the (MAD2D-CM)-MRR MATERIALES AVANZADOS-IMDEA-NC and (MAD2D-CM)-MRR MATERIALES AVANZADOS-UAM is acknowledged. M.G. has received financial support through the "Ramón y Cajal" Fellowship program (RYC2020-029317-I) and "Ayudas para Incentivar la Consolidación Investigadora" (CNS2022-135175). M. P. wishes to acknowledge partial support by Centro Nazionale di Ricerca in High-Performance Computing, Big Data and Quantum Computing, PNRR 4 2 1.4, CI CN00000013, CUP H23C22000360005. We acknowledge allocation of computing time at the Mare Nostrum Supercomputer of the Red Española de Supercomputación (BSC-RES) and the Centro de Computación Científica of the Universidad Autónoma de Madrid (CCC-UAM).

References

1 E. Mitterreiter, B. Schuler, A. Micevic, D. Hernangómez-Pérez, K. Barthelmi, K. A. Cochrane, J. Kiemle, F. Sigger, J. Klein, E. Wong, E. S. Barnard, K. Watanabe, T. Taniguchi, M. Lorke, F. Jahnke, J. J. Finley, A. M. Schwartzberg, D. Y. Qiu, S. Refaely-Abramson, A. W. Holleitner, A. Weber-Bargioni and C. Kastl, *Nat. Commun.*, 2021, **12**, 3822.

2 B. Schuler, D. Y. Qiu, S. Refaely-Abramson, C. Kastl, C. T. Chen, S. Barja, R. J. Koch, D. F. Ogletree, S. Aloni, A. M. Schwartzberg, J. B. Neaton, S. G. Louie and A. Weber-Bargioni, *Phys. Rev. Lett.*, 2019, **123**, 076801.

3 W. Zhu, T. Low, Y.-H. Lee, H. Wang, D. B. Farmer, J. Kong, F. Xia and P. Avouris, *Nat. Commun.*, 2014, **5**, 3087.

4 S. Barja, S. Refaely-Abramson, B. Schuler, D. Y. Qiu, A. Pulkin, S. Wickenburg, H. Ryu, M. M. Ugeda, C. Kastl, C. Chen, C. Hwang, A. Schwartzberg, S. Aloni, S.-K. Mo, D. Frank Ogletree, M. F. Crommie, O. V. Yazyev, S. G. Louie, J. B. Neaton and A. Weber-Bargioni, *Nat. Commun.*, 2019, **10**, 3382.

5 Y. J. Zheng, Y. Chen, Y. L. Huang, P. K. Gogoi, M.-Y. Li, L.-J. Li, P. E. Trevisanutto, Q. Wang, S. J. Pennycook, A. T. S. Wee and S. Y. Quek, *ACS Nano*, 2019, **13**, 6050–6059.

6 E. Mitterreiter, B. Schuler, A. Micevic, D. Hernangómez-Pérez, K. Barthelmi, K. A. Cochrane, J. Kiemle, F. Sigger, J. Klein, E. Wong, E. S. Barnard, K. Watanabe, T. Taniguchi, M. Lorke, F. Jahnke, J. J. Finley, A. M. Schwartzberg, D. Y. Qiu, S. Refaely-Abramson, A. W. Holleitner, A. Weber-Bargioni and C. Kastl, *Nat. Commun.*, 2021, **12**, 3822.

7 Z. Lin, B. R. Carvalho, E. Kahn, R. Lv, R. Rao, H. Terrones, M. A. Pimenta and M. Terrones, *2D Mater.*, 2016, **3**, 022002.

8 W. Zhou, X. Zou, S. Najmaei, Z. Liu, Y. Shi, J. Kong, J. Lou, P. M. Ajayan, B. I. Yakobson and J. C. Idrobo, *Nano Lett.*, 2013, **13**, 2615–2622.

9 C. J. Alvarez, M. T. Dau, A. Marty, C. Vergnaud, H. L. Poche, P. Pochet, M. Jamet and H. Okuno, *Nanotechnology*, 2018, **29**, 425706.

10 Z. Yan, M. Yoon and S. Kumar, *2D Mater.*, 2018, **5**, 031008.

11 B. Schuler, J. H. Lee, C. Kastl, K. A. Cochrane, C. T. Chen, S. Refaely-Abramson, S. Yuan, E. v. Veen, R. Roldán, N. J. Borys, R. Koch, S. Aloni, A. Schwartzberg, D. F. Ogletree, J. B. Neaton and A. Weber-Bargioni, *ACS Nano*, 2019, **13**, 10520–10534.

12 K. Teichmann, M. Wenderoth, S. Loth, R. G. Ulbrich, J. K. Garleff, A. P. Wijnheijmer and P. M. Koenraad, *Phys. Rev. Lett.*, 2008, **101**, 076103.

13 R. Zhang, G. Clark, X. Xu, P. T. Darancet and J. R. Guest, *J. Phys. Chem. C*, 2021, **125**, 14056–14064.

14 M. Fu, L. Liang, Q. Zou, G. D. Nguyen, K. Xiao, A.-P. Li, J. Kang, Z. Wu and Z. Gai, *J. Phys. Chem. Lett.*, 2020, **11**, 740–746.

15 G. D. Nguyen, L. Liang, Q. Zou, M. Fu, A. D. Oyedele, B. G. Sumpter, Z. Liu, Z. Gai, K. Xiao and A.-P. Li, *Phys. Rev. Lett.*, 2018, **121**, 086101.

16 I. D. Bernardo, J. Blyth, L. Watson, K. Xing, Y. H. Chen, S. Y. Chen, M. T. Edmonds and M. S. Fuhrer, *J. Phys.: Condens. Matter*, 2022, **34**, 174002.

17 J. Coraux, A. T. N'Diaye, C. Busse and T. Michely, *Nano Lett.*, 2008, **8**, 565–570.

18 J. Ripoll-Sau, F. Calleja, P. Casado Aguilar, I. M. Ibarburu, A. L. Vázquez de Parga, R. Miranda and M. Garnica, *Nanoscale*, 2022, **14**, 10880–10888.

19 I. Horcas, R. Fernández, J. M. Gómez-Rodríguez, J. Colchero, J. Gómez-Herrero and A. M. Baro, *Rev. Sci. Instrum.*, 2007, **78**, 013705.

20 D. Nečas and P. Klapetek, *Cent. Eur. J. Phys.*, 2012, **10**, 181–188.

21 P. E. Blöchl, *Phys. Rev. B: Condens. Matter Mater. Phys.*, 1994, **50**, 17953–17979.

22 G. Kresse and D. Joubert, *Phys. Rev. B: Condens. Matter Mater. Phys.*, 1999, **59**, 1758–1775.

23 G. Kresse and J. Furthmüller, *Comput. Mater. Sci.*, 1996, **6**, 15–50.

24 G. Kresse and J. Furthmüller, *Phys. Rev. B: Condens. Matter Mater. Phys.*, 1996, **54**, 11169–11186.

25 J. P. Perdew, K. Burke and M. Ernzerhof, *Phys. Rev. Lett.*, 1996, **77**, 3865–3868.

26 A. Tkatchenko and M. Scheffler, *Phys. Rev. Lett.*, 2009, **102**, 073005.

27 M. Pisarra, C. Díaz and F. Martín, *Phys. Rev. B*, 2021, **103**, 195416.

28 C. Mallika and O. Sreedharan, *J. Chem. Thermodyn.*, 1988, **20**, 769–775.

29 M. Batzill, *J. Phys.: Condens. Matter*, 2018, **30**, 493001.

30 P. M. Coelho, H. P. Komsa, H. C. Diaz, Y. Ma, A. V. Krasheninnikov and M. Batzill, *ACS Nano*, 2018, **12**, 3975–3984.

31 L. Wang, Y. Wu, Y. Yu, A. Chen, H. Li, W. Ren, S. Lu, S. Ding, H. Yang, Q. K. Xue, F. S. Li and G. Wang, *ACS Nano*, 2020, **14**, 8299–8306.

32 S. Barja, S. Wickenburg, Z.-F. Liu, Y. Zhang, H. Ryu, M. Ugeda, Z. Hussain, Z.-X. Shen, S.-K. Mo, E. Wong, M. Salmeron, F. Wang, M. F. Crommie, D. F. Ogletree, J. Neaton and A. Weber-Bargioni, *Nat. Phys.*, 2016, **12**, 751–756.

33 W. Jolie, C. Murray, P. S. Weiß, J. Hall, F. Portner, N. Atodiresei, A. V. Krasheninnikov, C. Busse, H.-P. Komsa, A. Rosch and T. Michely, *Phys. Rev. X*, 2019, **9**, 011055.

34 Y. Xia, J. Zhang, Y. Jin, W. Ho, H. Xu and M. Xie, *ACS Nano*, 2020, **14**, 10716–10722.

35 T. Zhu, W. Ruan, Y. Q. Wang, H. Z. Tsai, S. Wang, C. Zhang, T. Wang, F. Liou, K. Watanabe, T. Taniguchi, J. B. Neaton, A. Weber-Bargioni, A. Zettl, Z. Q. Qiu, G. Zhang, F. Wang, J. E. Moore and M. F. Crommie, *Nat. Mater.*, 2022, **21**, 748–753.

36 C.-L. Song, Y.-P. Jiang, Y.-L. Wang, Z. Li, L. Wang, K. He, X. Chen, X.-C. Ma and Q.-K. Xue, *Phys. Rev. B: Condens. Matter Mater. Phys.*, 2012, **86**, 045441.

37 M. T. Edmonds, J. L. Collins, J. Hellerstedt, I. Yudhistira, L. C. Gomes, J. N. B. Rodrigues, S. Adam and M. S. Fuhrer, *Sci. Adv.*, 2017, **3**, eaao6661.

38 V. W. Brar, R. Decker, H.-M. Solowan, Y. Wang, L. Maserati, K. T. Chan, H. Lee, a. O. Girit, A. Zettl, S. G. Louie, M. L. Cohen and M. F. Crommie, *Nat. Phys.*, 2011, **7**, 43–47.

39 L. Liu, T. Dienel, R. Widmer and O. Gröning, *ACS Nano*, 2015, **9**, 10125–10132.

40 M. Pörtner, Y. Wei, A. Riss, K. Seufert, M. Garnica, J. V. Barth, A. P. Seitsonen, L. Diekhöner and W. Auwärter, *Adv. Mater. Interfaces*, 2020, **7**, 2000080.

41 H. Liu, H. Zheng, F. Yang, L. Jiao, J. Chen, W. Ho, C. Gao, J. Jia and M. Xie, *ACS Nano*, 2015, **9**, 6619–6625.

42 C. G. Van de Walle and J. Neugebauer, *J. Appl. Phys.*, 2004, **95**, 3851–3879.

43 G. V. Nazin, X. H. Qiu and W. Ho, *Phys. Rev. Lett.*, 2005, **95**, 1–4.

44 N. Fukata, A. Kasuya and M. Suezawa, *Phys. B*, 2001, **308–310**, 1125–1128.

45 J. J. Navarro, M. Pisarra, B. Nieto-Ortega, J. Villalva, C. G. Ayani, C. Díaz, F. Calleja, R. Miranda, F. Martín, E. M. Pérez and A. Vázquez de Parga, *Sci. Adv.*, 2018, **4**, eaau9366.

46 J. Hall, B. Pielić, C. Murray, W. Jolie, T. Wekking, C. Busse, M. Kralj and T. Michely, *2D Mater.*, 2018, **5**, 025005.